






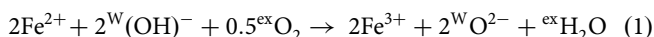
## Atomistic insight into lithospheric conductivity revealed by phonon–electron excitations in hydrous iron-bearing silicates

Boriana Mihailova <sup>1✉</sup>, Giancarlo Della Ventura <sup>2,3</sup>, Naemi Waesermann<sup>1</sup>, Wei Xu<sup>4</sup>, Jochen Schlüter<sup>5</sup>, Federico Galdenzi<sup>2,3</sup>, Augusto Marcelli<sup>3,6</sup>, Günther J. Redhammer <sup>7</sup>, Massimo Boiocchi <sup>8</sup> & Roberta Oberti <sup>9</sup>

Amphiboles are essential components of the continental crust and subduction zones showing anomalous anisotropic conductivity. Rock properties depend on the physical properties of their constituent minerals, which in turn depend on the crystal phonon and electron density of states. Here, to address the atomic-scale mechanism of the peculiar rock conductivity, we applied in situ temperature-dependent Raman spectroscopy, sensitive to both phonon and electron states, to Fe<sup>2+</sup>-rich amphiboles. The observed anisotropic resonance Raman scattering at elevated temperatures, in combination with density-functional-theory modelling, reveals a direction-dependent formation of mobile polarons associated with coupled FeO<sub>6</sub> phonons and electron transitions. Hence, temperature-activated electron-phonon excitations in hydrous iron-bearing chain and layered silicates are the atomistic source of anisotropic lithospheric conductivity. Furthermore, reversible delocalization of H<sup>+</sup> occurs at similar temperatures even in a reducing atmosphere. The occurrence of either type of charge carriers does not require initial mixed-valence state of iron or high oxygen fugacity in the system.

<sup>1</sup>FB Erdsystemwissenschaften, Universität Hamburg, Hamburg, Germany. <sup>2</sup>Dipartimento di Scienze, Università di Roma Tre, Largo S, Rome, Italy. <sup>3</sup>INFN Laboratori Nazionali di Frascati, Frascati, Italy. <sup>4</sup>Beijing Synchrotron Radiation Facility, Institute of High Energy Physics, Chinese Academy of Sciences, Beijing, China. <sup>5</sup>Centrum für Naturkunde, Universität Hamburg, Hamburg, Germany. <sup>6</sup>RICMASS, Rome, Italy. <sup>7</sup>Department of Chemistry and Physics of Materials, University of Salzburg, Salzburg, Austria. <sup>8</sup>Centro Grandi Strumenti, Università di Pavia, Pavia, Italy. <sup>9</sup>CNR-Istituto di Geoscienze e Georisorse, Sede Secondaria di Pavia, Pavia, Italy. ✉email: [boriana.mihalova@uni-hamburg.de](mailto:boriana.mihalova@uni-hamburg.de)

**A**mphiboles, hydrous silicates with the general formula  $AB_2C_5T_8O_{22}W_2$ <sup>1</sup>, are very important constituents of the Earth's lithosphere, occurring in a diversity of rock types<sup>2</sup>. Being a structural bridge between pyroxenes and phyllosilicates, amphiboles are involved in a number of transformation processes at elevated temperatures and pressures during subduction. The ultimate effects of these processes include the oxidation of Fe and the release of water into the lower crust/mantle<sup>3,4</sup>. The strong structural anisotropy of the amphiboles results in heavily anisotropic elastic, thermoelastic, dielectric, and conductivity properties, which in turn contributes to the behavior of the host rock. The amphibole structure (see Fig. 1a) may accommodate a variety of chemical elements at the non-tetrahedrally coordinated crystallographic sites:  $M(1)$ ,  $M(2)$ , and  $M(3)$  occupied by C-type cations, as well as at the  $M(4)$  site occupied by B-type cations, which strongly influences their properties and thermal stability<sup>5</sup>. A particularly important issue in the crystal chemistry of these minerals is the stability of Fe-bearing species, because their oxidation processes have a paramount importance in a wide spectrum of fields, including geology and geophysics, but also materials science and toxicology<sup>6,7</sup>. Early *ex situ* work<sup>8,9</sup> have revealed that oxidation of  ${}^C\text{Fe}$  is intrinsically coupled with a loss of hydrogen from the hydroxyl group, in the presence of external oxygen ( ${}^{\text{ex}}\text{O}_2$ ), according to the reaction:

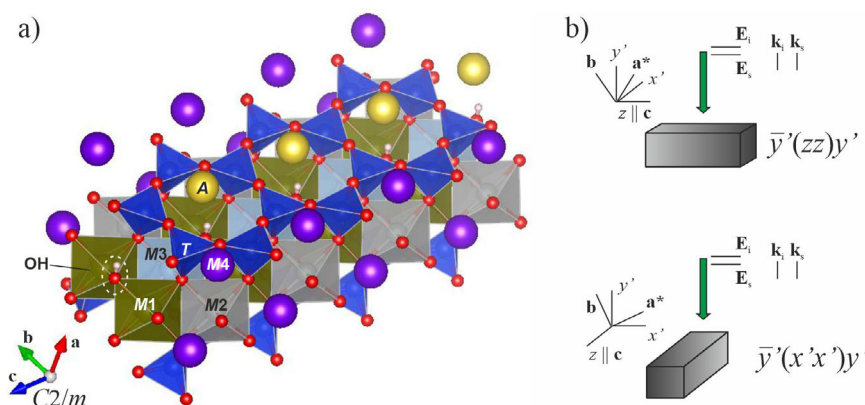


Further *in situ* studies have clarified the changes in the interatomic distances and site population associated with iron oxidation as well as the subsequent phase transformations<sup>5,10,11</sup>. Very recently, by combining diffraction and spectroscopic methods, thus probing the structure at different length and time scales, it has been shown that the above simple chemical reaction is preceded by multiple local-scale structural changes<sup>12–15</sup>. A particularly important issue, which has been achieved mainly via Raman spectroscopy, is the existence of a thermal state of reversible dynamic oxidation. This state consists of delocalization of electrons  $e^-$  from the octahedrally coordinated iron cations as well as of  $\text{H}^+$  from the W-type anions<sup>13</sup>. For temperatures within the range of dynamic oxidation, both  $e^-$  and  $\text{H}^+$  remain inside the crystal bulk but if the temperature decreases, they can be attached back to  ${}^C\text{Fe}^{3+}$  and  ${}^W\text{O}^{2-}$ , respectively, to form again  ${}^C\text{Fe}^{2+}$  and  ${}^W(\text{OH})^-$ . Only when the thermal energy is high enough, the atomic vibrations trigger a readjustment of the  $\text{TO}_4$ -ring geometry to match with smaller-size adjacent  $\text{MO}_6$  octahedra (see

Fig. 1a), which in turn allows for the irreversible  $\text{Fe}^{2+} \rightarrow \text{Fe}^{3+}$  exchange and release of  $\text{H}^+$  cations from the amphibole structure<sup>13</sup>.

The delocalization of  $e^-$  and  $\text{H}^+$  and consequent hopping within the amphibole structure results in an increase in mineral conductivity<sup>14,16</sup>, a feature that may have a tremendous impact on the physics of hydrous silicates with a quasi one-dimensional structure and on potential mineral-inspired technologies<sup>6</sup>. Moreover, the possible development of transport and magnetic properties in iron-bearing amphiboles at elevated temperatures is of extreme interest in geophysics<sup>17–20</sup>, especially when modeling lithospheric conductivity<sup>16,21</sup>. For the latter, dehydrogenation of amphiboles and other representative hydrous silicates is also considered to play an important role for the high-temperature anomalies in subduction zones<sup>22</sup>. Besides, the dehydrogenation of amphiboles and related layered silicates can contribute to the water cycling at depth or, depending on the local rock assemblages, to the formation of abiotic  $\text{H}_2$  and  $\text{CH}_4$ <sup>23</sup>.

So far, studies on the stability of Fe-containing amphiboles have been mainly restricted to species from the sodium amphibole subgroup (e.g., ref. 13 and references therein), which are typical of high-pressure rocks. However, given the large compositional variety of amphiboles, it is important to study the high-temperature behavior of different amphibole subgroups, in order to understand whether the state of existing charge carriers in terms of delocalized  $e^-$  and  $\text{H}^+$  is a general property of all amphiboles. Hence, we have analyzed grunerite, ideally  ${}^A\text{BFe}^{2+}{}^C\text{Fe}^{2+}{}^5\text{Si}_8\text{O}_{22}(\text{OH})_2$ , a member of the magnesium-iron-manganese amphibole subgroup<sup>24</sup>. These species are particularly common in metamorphic rocks, where they may coexist with amphiboles of the tremolite-actinolite series or with serpentine-group minerals<sup>2</sup>. Amphiboles belonging to the Mg-Fe-Mn subgroup may crystallize in orthorhombic ( $Pnma$  or  $Pnmm$ ) or monoclinic ( $C2/m$  or  $P2_1/m$ ) symmetry. The monoclinic structure is stabilized if  $\text{Fe}^{2+}$  dominates both as B- and as C-type cation<sup>25</sup>. In Mg-dominant amphiboles, a reversible displacive  $P2_1/m$ -to- $C2/m$  phase transition may occur on heating<sup>5</sup>, with a critical temperature  $T_c$  decreasing from  $\sim 600$  to  $\sim 200$  K, with the increase of  $\text{Fe}^{2+}$  content<sup>5,26</sup>. Very recently, we have demonstrated the possibility of discriminating the crystal system of Mg-Fe-Mn and Li amphiboles by the position of a low-wavenumber Raman peak, which appears at  $\sim 75$ – $85$   $\text{cm}^{-1}$  and  $\sim 60$ – $70$   $\text{cm}^{-1}$  for monoclinic and orthorhombic amphiboles, respectively<sup>27</sup>. Similarly to pyroxenes<sup>28</sup>, this peak is assigned to an external  $\text{TO}_4$



**Fig. 1 Amphibole structure and scattering geometries.** **a** Fragment of the structure of a  ${}^W(\text{OH})$ -amphibole with  $C2/m$  symmetry;  $\text{TO}_4$  tetrahedra are given in blue, whereas  $M(1)\text{O}_6$ ,  $M(2)\text{O}_6$ , and  $M(3)\text{O}_6$  octahedra in olive-greenish, gray, and light-bluish, respectively. Large yellow and violet spheres represent the A- and  $M(4)$ -site cations; the small red spheres are the oxygen atoms. The dashed ellipse marks a  ${}^W(\text{OH})^-$  group. The figure was prepared using the VESTA software package<sup>51</sup>. **b** Sketch of the experimental geometry used in the Raman scattering experiments. **a–c** are the fundamental translation vectors of  $C2/m$  in the direct space, **a\*** in the reciprocal space, i.e. **a\* $\perp$ b $\perp$ c**.

mode of the silicate double chain, and mirrors the relative geometry of the silicate anion with respect to small eight-coordinated (B-type) cations. For this reason, it is expected to be sensitive to temperature-driven phase transitions that are strongly controlled by the B-site size<sup>5</sup>.

Here, we report the results of our temperature-dependent polarized Raman spectroscopic study of grunerite heated in air or in N<sub>2</sub> atmosphere, to follow the dynamics of multistep oxidation processes and the temperature-induced structural transformations. The most striking result is the existence of a strongly anisotropic reversible oxidation mechanism even under reducing atmosphere, which consists in direction-dependent coupled electron-phonon transition at elevated temperatures. Such temperature-induced conduction electrons associated with FeO<sub>6</sub> octahedra, in the presence of delocalized H<sup>+</sup>, should be a universal property of all one-dimensional or two-dimensional Fe-bearing hydrous silicates. This phenomenon provides insights into the atomistic driving force for the increasing conductivity observed in subducted rocks at convergent plate margins<sup>16</sup>.

## Results

**Symmetry considerations, anomalous anisotropic Raman scattering, and selection rules.** Two natural grunerite samples, designated as A85 and A86<sup>27</sup> and with chemical formulae given in Table 1, have been studied by in situ temperature-dependent Raman spectroscopy. At each temperature parallel polarized spectra (incident-light polarization E<sub>i</sub> parallel to the scattered-light polarization E<sub>s</sub>) were collected in backscattering geometry (the direction of propagation of the incident light, k<sub>i</sub>, is anti-parallel to the direction of propagation of the scattered light, k<sub>s</sub>) from a natural crystal face in two different orientations of the crystal grain, i.e., with the crystallographic c axis parallel to E<sub>i</sub> and the c axis perpendicular to E<sub>i</sub>. In Porto's notation, k<sub>i</sub>(E<sub>i</sub>E<sub>s</sub>)k<sub>s</sub>, the former geometry corresponds to  $\bar{y}(zz)y'$ , whereas the latter to  $\bar{y}(x'x')y'$ , where z is along the c axis and x' and y' are two mutually perpendicular directions within the (a\*,b) plane (see the sketch in Fig. 1b). In both geometries only A<sub>g</sub> modes are observed, whose Raman polarizability tensor in 2/m point symmetry is given by<sup>29</sup>:

$$\alpha(A_g) = \begin{pmatrix} \alpha_{xx} & \cdot & \alpha_{xz} \\ \cdot & \alpha_{yy} & \cdot \\ \alpha_{xz} & \cdot & \alpha_{zz} \end{pmatrix} \quad (2)$$

Therefore, the  $\bar{y}(zz)y'$  spectra are dominated by the  $\alpha_{zz}$  component, whereas the  $\bar{y}(x'x')y'$  spectra are determined either by both  $\alpha_{xx}$  and  $\alpha_{yy}$  components or only by  $\alpha_{xx}$  depending on whether the crystal-grain face is parallel to {110} or {010} cleavage plane.

Selected  $\bar{y}(zz)y'$  in situ Raman spectra of near-end-member grunerite A85 in air are shown in Fig. 2a. The overall Raman scattering drastically changes above 650 K: new broad peaks appear at ~273, 470, 576, and 815 cm<sup>-1</sup>, whereas all symmetry-allowed first-order Raman peaks are suppressed, and above 750 K they cannot be resolved any longer. The only exception is the

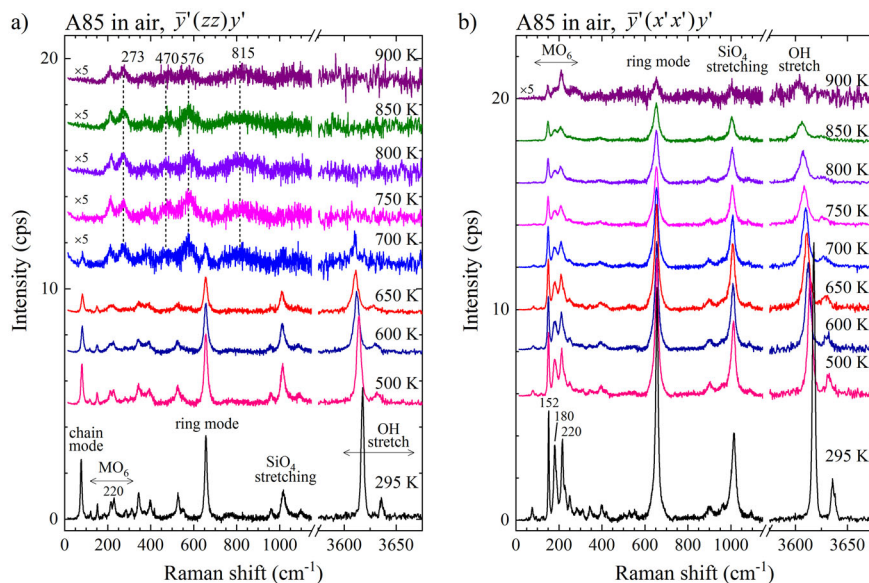
Raman-active MO<sub>6</sub> mode that at room temperature generates a doublet ~220 cm<sup>-1</sup>. Note that in  $\bar{y}(zz)y'$  geometry, the polarization of the incident light E<sub>i</sub> is parallel to the crystallographic c axis. The temperature evolution of the Raman scattering is totally different when collected with E<sub>i</sub> ⊥ c, i.e., in  $\bar{y}(x'x')y'$  geometry (Fig. 2b): on heating from 295 to 850 K all Raman-active phonon modes are well preserved, gradually decreasing in wavenumber and increasing in width, as it should be expected for crystals with a positive volume thermal expansion and no phase transitions. Only at 900 K the signal-to-noise ratio degrades and the Raman scattering generated by the MO<sub>6</sub> vibrations ~220 cm<sup>-1</sup> is enhanced, but the overall Raman scattering characteristic of amphiboles is still retained. The  $\bar{y}(x'x')y'$  spectra thus show that the amphibole structure is stable at least up to 900 K and therefore, the change in the selection rules observed in  $\bar{y}(zz)y'$  geometry at elevated temperatures cannot be related to a structural transformation. Here, we should recall that the Raman scattering of solids is a light-matter interaction process that depends not only on the equilibrium configuration of nuclei, but also on the electron density of states (DOS). In the case of non-metallic materials, if the photon energy of the excitation laser line E<sub>photon</sub> is smaller than the electron energy gap E<sub>g</sub>, the selection rules are determined only by the phonon wave functions. However, when E<sub>photon</sub> is close to or larger than E<sub>g</sub>, the incoming photon can excite simultaneously a phonon and an electron, and the selection rules under such resonance conditions depend on both the phonon and the electron wave functions. For insulating and semiconducting materials, the resonance Raman scattering (RRS) is achieved via the so-called Fröhlich interactions<sup>30</sup>, consisting in electrostatic interactions between electrons and longitudinal optical (LO) polar phonons. In the case of centrosymmetrical crystals as C2/m amphiboles, under non-resonance conditions (i.e., no electron transitions) the polar phonons at the Brillouin zone center are infrared-active but Raman inactive, and vice versa. Therefore, the optical phonon modes that are Raman-active under non-resonance conditions cannot participate in Fröhlich interactions because they do not carry polarity and can become forbidden under resonance conditions (i.e., when electron transitions are activated by a photon or another external stimulus)<sup>31</sup>. Moreover, the RRS owing to Fröhlich interactions is selective; a resonance enhancement is expected only for those LO polar phonons that are related to the local structural species in which the electron transition occurs and therefore can couple with the excited electron<sup>31–33</sup>.

**Assignment of the observed spectral features at elevated temperatures.** In our experiment, we changed the temperature, maintaining constant the excitation wavelength (λ = 514.532 nm). Actually, the temperature at which we observe drastic changes in the spectra is ~700 K, which is equivalent to ~0.06 eV, well below the photon energy of 2.4 eV corresponding to λ = 514.532 nm. Hence, the puzzling picture observed for grunerite (Fig. 2) can only be explained by temperature-activated electron transitions across E<sub>g</sub> that interact with polar optical phonons, forming strongly anisotropic

**Table 1 Crystal-chemical formulae, obtained by combining electron-microprobe, XRD, and Mössbauer analyses, and space-group symmetry at room temperature for the studied samples; elements with <0.005 atoms per formula unit (apfu) were neglected.**

Sample	A <sup>B</sup> [M(4)] <sub>2</sub> C <sup>C</sup> [M(1) <sub>2</sub> M(2) <sub>2</sub> M(3)]T <sub>8</sub> O <sub>22</sub> W <sub>2</sub>	Symmetry
A85	A <sup>B</sup> [M(4)] <sub>2</sub> (Fe <sup>2+</sup> <sub>1.96</sub> Mg <sub>0.02</sub> Ca <sub>0.01</sub> Na <sub>0.01</sub> ) <sup>C</sup> [M(1)(Fe <sup>2+</sup> <sub>1.84</sub> Mg <sub>0.16</sub> ) <sup>M(2)</sup> (Fe <sup>2+</sup> <sub>1.76</sub> Mg <sub>0.21</sub> Al <sub>0.03</sub> ) <sup>M(3)</sup> (Fe <sup>2+</sup> <sub>0.94</sub> Mg <sub>0.06</sub> )] <sup>T</sup> (Si <sub>7.97</sub> Al <sub>0.03</sub> )O <sub>22</sub> <sup>W</sup>	C2/m
A86	A <sup>B</sup> [M(4)] <sub>2</sub> (Fe <sup>2+</sup> <sub>1.87</sub> Ca <sub>0.10</sub> Mn <sub>0.01</sub> Na <sub>0.02</sub> ) <sup>C</sup> [M(1)(Fe <sup>2+</sup> <sub>1.48</sub> Mg <sub>0.52</sub> ) <sup>M(2)</sup> (Fe <sup>2+</sup> <sub>1.17</sub> Mg <sub>0.79</sub> Al <sub>0.04</sub> ) <sup>M(2)</sup> (Fe <sup>2+</sup> <sub>0.78</sub> Mg <sub>0.22</sub> )] <sup>T</sup> (Si <sub>7.97</sub> Al <sub>0.03</sub> )O <sub>22</sub> <sup>W</sup>	C2/m

No traces of Fe<sup>3+</sup> were detected by Mössbauer spectroscopy in either sample.



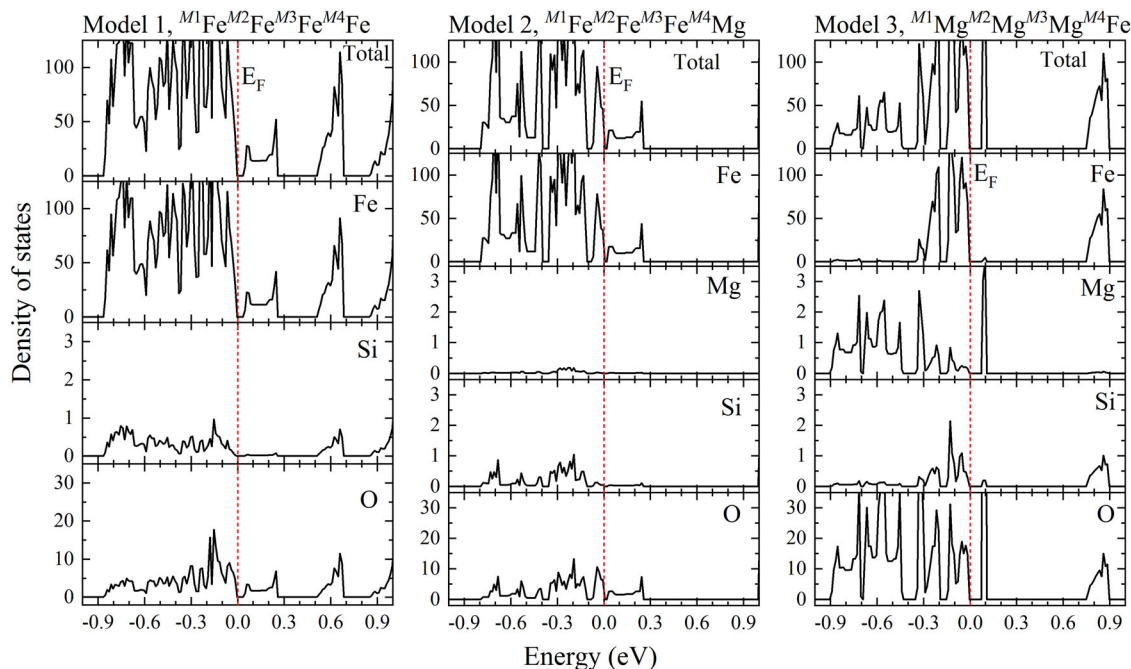
**Fig. 2** Temperature-dependent polarized Raman spectra of grunerite A85 measured in situ in air. **a** Data collected in  $\bar{y}'(zz)y'$  scattering geometry; **b** data collected in  $\bar{y}'(x'x')y'$  scattering geometry. The dashed lines trace the new Raman scattering signals appearing at 700 K in  $\bar{y}'(x'x')y'$  spectra. The mode assignment follows the arguments given in refs. 27,52. Spectra are vertically offset for clarity.

intrinsic local polarizations  $P_{\text{loc}}$ , i.e., mobile polarons with aligned dipole moments. These temperature-activated coupled electron–phonon excitations will change the Raman selection rules from non-resonant to resonant only when  $P_{\text{loc}}$  is parallel to the photon polarization  $E_p$ , to fulfill the requirement for three-particle interaction among the excited electron, the phonon, and the incoming photon. When  $P_{\text{loc}}$  is perpendicular to  $E_p$ , the temperature-induced polaron dipole moments do not interact with the photon polarization and hence the inelastic light scattering is realized only via photon–phonon interaction. This causes the appearance of RRS only in  $\bar{y}'(zz)y'$  scattering geometry, while the  $\bar{y}'(x'x')y'$  spectra still correspond to non-resonant selection rules. All phonons related to the silicate anion, including the  $\text{SiO}_4$  stretching modes  $\sim 900\text{--}1100\text{ cm}^{-1}$ , the  $\text{SiO}_4$ -ring mode  $\sim 658\text{ cm}^{-1}$ , the  $\text{SiO}_4$ -chain mode  $\sim 78\text{ cm}^{-1}$ , as well as the OH-stretching modes are suppressed under resonance conditions (see Fig. 2a). In contrast, phonons involving vibrations of  $\text{MO}_6$  octahedra, e.g.,  $\sim 220\text{ cm}^{-1}$ <sup>27,34</sup>, are resonantly enhanced. Moreover, the most pronounced resonantly activated phonon mode appears  $\sim 570\text{ cm}^{-1}$ , a wavenumber that is typical of  $\text{Fe}^{3+}\text{O}_6$  stretching in  $\text{CFe}$ -bearing amphiboles<sup>27,34</sup>. Therefore, the electron transition responsible for the anisotropic RRS occurs between electron levels related to the  $\text{FeO}_6$  octahedra and has an induced dipole moment parallel to the  $c$  axis. Because of such a transition, conduction electrons form in the crystal and locally, the oxidation state of the corresponding  $\text{CFe}^{n+}$  ions changes from divalent to trivalent. This being the case, the direction-preferred formation of conduction electrons at elevated temperatures is expected to be an intrinsic feature of all amphiboles containing octahedrally coordinated Fe, allowing for polaron mobility associated with the strips of octahedra. Note that the temperature above which we observe this phenomenon is consistent with the requirement that the threshold temperature of small polaron hopping is about half the Debye temperature of the system<sup>35–37</sup>.

To verify our conclusions, density-functional theory (DFT) calculations were performed on three model systems with the same structure, using that of A85, but having different occupancy at the  $M(1)$ ,  $M(2)$ ,  $M(3)$ , and  $M(4)$  sites: (i) all sites occupied by  $\text{Fe}^{2+}$ , (ii) octahedrally coordinated  $M(1\text{--}3)$  sites occupied by  $\text{Fe}^{2+}$ , and  $M(4)$  by Mg, and (iii) octahedrally coordinated  $M(1\text{--}3)$  sites occupied by Mg, and  $M(4)$  by  $\text{Fe}^{2+}$ . The projected electron DOS

for Fe, O, Si, and Mg in different models is shown in Fig. 3. The calculated energy gap for end-member grunerite (where  $M(1)M(2)M(3)M(4) = \text{FeFeFeFe}$ ) is  $E_g = 0.05\text{ eV}$  (see Supplementary Figure 8 and Supplementary Table 5), close to the value of  $0.06\text{ eV}$  suggested from the experiment, although one should keep in mind that in general only semi-quantitative conclusions can be gained from DFT calculations. The projected DOS for the two imaginary compounds  $(M(1)M(2)M(3)M(4) = \text{FeFeFeMg})$  and  $(M(1)M(2)M(3)M(4) = \text{MgMgMgFe})$  clearly show that Fe at  $M(1\text{--}3)$  contributes to the conduction band between  $\sim 0.001$  and  $0.02\text{ eV}$ , whereas Fe at  $M(4)$  to that  $\sim 0.6\text{ eV} \Leftrightarrow \sim 6900\text{ K}$ . Therefore, we can safely state that the experimentally observed phenomena  $\sim 700\text{ K}$  are exclusively related to octahedrally coordinated Fe. Moreover, the orbital DOSs of Fe as well as of O atoms from the  $\text{MO}_6$ -strip (see Supplementary Figures 2–7) suggest that the top of the valence band results from the hybridization between O  $2p_x$  orbitals and Fe  $3d_{xy}$  orbitals, whereas the bottom of the conduction band from the hybridization between O  $2p_x$  and Fe  $d_{x^2-y^2}$  orbitals. Therefore, the dipole moment related to electron transitions across  $E_g$  is along  $z$  (parallel to the crystallographic  $c$  axis), in full agreement with the conclusions derived from the experimentally observed anisotropic appearance of RRS.

**Quantitative trends from heating experiments on near-end-member grunerite (A85) in air.** The Raman spectra of A85 measured in air at room temperature after annealing the sample at different temperatures (Fig. 4) show an almost total recovery of the  $\bar{y}'(zz)y'$  scattering after heating up to 700 K. The non-RRS peaks, however, are gradually suppressed after heating up to 750 K and 800 K, and completely disappear after heating at 850 and 900 K. This trend can be quantified by the intensity ratio  $I_{586}^{\text{RRS}}/(I_{586}^{\text{RRS}} + I_{\text{ring mode}})$ , i.e., the relative intensity between the strongest RRS peak  $\sim 586\text{ cm}^{-1}$  and the strongest non-RRS peak generated by framework vibrations, namely the ring mode  $\sim 658\text{ cm}^{-1}$ . Figure 4a demonstrates that the experimental data plotted versus the heating temperature follow a Boltzmann growth function with an inflection at  $T_{\text{heat}}^{\text{inf}} = 720\text{ K}$ . This value matches exactly the transition temperature obtained by X-ray diffraction (XRD) and X-ray absorption spectroscopy for the closely related



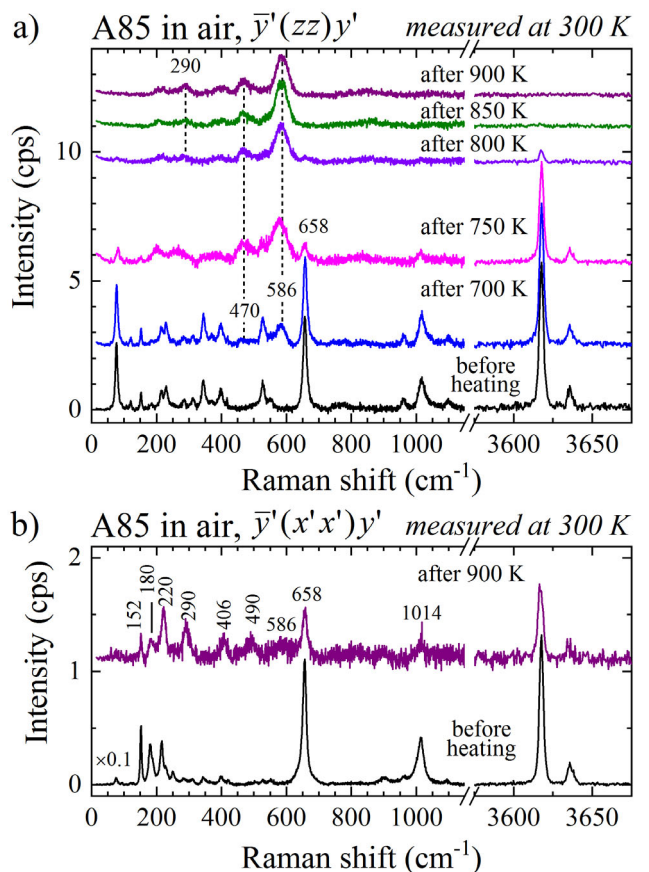
**Fig. 3 Electron density of states.** The total and projected electron densities of states are calculated for  $M(1)M(2)M(3)M(4) = \text{Fe}^{2+}\text{Fe}^{2+}\text{Fe}^{2+}\text{Fe}^{2+}$  (Model 1),  $M(1)M(2)M(3)M(4) = \text{Fe}^{2+}\text{Fe}^{2+}\text{Fe}^{2+}\text{Mg}$  (Model 2), and  $M(1)M(2)M(3)M(4) = \text{MgMgMgMgFe}^{2+}$  (Model 3); the red dashed lines mark the Fermi energy set at 0 eV.

amphibole riebeckite<sup>11,15</sup>, which further emphasizes that the irreversible RRS is related to permanent Fe oxidation. In our previous studies on riebeckite<sup>13</sup> we showed that the  $\text{MO}_6$  mode  $\sim 146 \text{ cm}^{-1}$  in  $\bar{y}'(x'x')y'$  spectra is sensitive to Fe oxidation; the fractional intensity of this mode increased in the temperature range of reversible oxidation (delocalization of  $e^-$  within the crystal bulk) and dropped abruptly on the verge of irreversible oxidation (ejection of  $e^-$  from the crystal). The same feature is observed here. In the spectra of grunerite, the corresponding  $\text{MO}_6$  mode occurs  $\sim 152 \text{ cm}^{-1}$ ; it shows a reduction of the relative intensity in the room-temperature spectrum collected after annealing the sample at 900 K (see Fig. 4b), indicating a partial irreversible oxidation. The analysis of the temperature dependence of this mode shows a perceptible increase in the fractional intensity at 720 K and an abrupt decrease above 850 K (see Fig. 5b), marking the beginning of reversible and irreversible oxidation, respectively. These two temperatures match very well  $T_{\text{heat}}^{\text{inf}}$  and  $T_{\text{heat}}$  for which room-temperature non-RRS modes completely disappears ( $I_{586}^{\text{RRS}}/(I_{586}^{\text{RRS}} + I_{\text{ring mode}}) = 1$ ). The irreversible enhancement of the Raman scattering  $\sim 220 \text{ cm}^{-1}$  relative to the signal at  $180 \text{ cm}^{-1}$  in the  $\bar{y}'(x'x')y'$  spectrum (see Fig. 4b) should also be related to irreversible Fe oxidation, similar to the intensity ratio of the doublet  $\sim 165\text{--}175 \text{ cm}^{-1}$  in the Raman spectra of riebeckite<sup>13</sup>. All this indicates strong correlation between the anisotropic RRS and the irreversible  $\text{Fe}^{2+} \rightarrow \text{Fe}^{3+}$  exchange, as the latter is the reason for quenched RRS at room temperature.

**In situ high-temperature experiments of near-end-member grunerite (A85) in  $\text{N}_2$ .** In order to determine whether the presence of  $\text{exO}_2$  is a necessary precondition for the anisotropic development of conduction (delocalized) electrons, we performed in situ Raman experiments purging the sample chamber with  $\text{N}_2$ . Figure 6 shows that reversible anisotropic RRS appears also under reducing atmosphere, but at higher temperatures than in air. Therefore, the presence of  $\text{exO}_2$  favors the direction-preferred electron transition between the hybridized O  $2p$  and Fe  $3d$  levels,

but it is not required for this process to occur. Hence, anisotropic conductivity due to mobile electrons can exist in amphiboles at elevated temperatures, independently of the external environment. Another interesting observation is that above 700 K the OH-stretching peaks can hardly be resolved in either scattering geometry, but they fully recover on cooling back to room temperature, emphasizing that the reversible delocalization of  $\text{WH}^+$  at high temperatures is also unaffected by the absence of  $\text{exO}_2$ . The diffusion of these delocalized  $\text{H}^+$  cations through the crystal bulk should also contribute to the overall electrical conductivity of amphiboles. The room-temperature  $\bar{y}'(x'x')y'$  spectra before and after heating in  $\text{N}_2$  are identical, whereas there are weak extra peaks  $\sim 583$  and  $464 \text{ cm}^{-1}$  in the  $\bar{y}'(zz)y'$  spectrum measured at room temperature after heating in  $\text{N}_2$  up to 800 K. The same is observed in the  $\bar{y}'(zz)y'$  spectrum measured at room temperature after heating up to 700 K in air (see Fig. 4a). Note that in both cases the ratio between the total integrated intensity generated by OH-stretching vibrations and by the framework vibrations (below  $1200 \text{ cm}^{-1}$ ) remains unchanged within uncertainties, confirming negligible loss of  $\text{H}^+$  upon heating to 800 K in  $\text{N}_2$  or 700 K in air. Therefore, for charge-balance reasons, there should be no ejection of electrons from the crystal bulk. On the other hand, the extra peaks are indicative of presence of  $\text{CFe}^{3+}$ <sup>27,34</sup>. This suggests that on cooling a small amount of temperature-activated conduction electrons have been trapped in deep defect levels and hence, some octahedrally coordinated iron ions could not recover their initial divalent oxidation state.

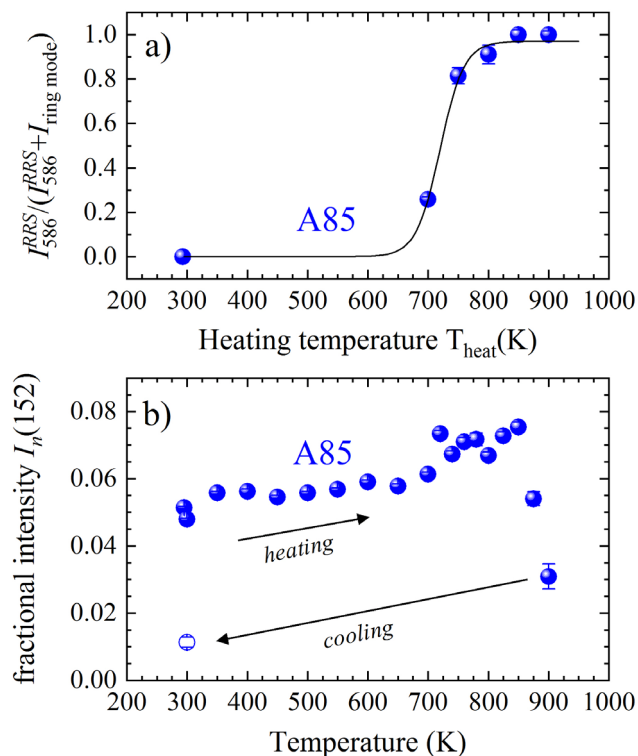
**Comparative analysis of the temperature behavior of the two grunerite samples.** The Raman scattering analysis of A86, which contains less  $\text{Fe}^{2+}$  than A85 (see Table 1), reveals the same temperature-induced processes as in A85. However, they occur at temperatures  $\sim 100 \text{ K}$  higher than the corresponding temperatures for A85. Reversible anisotropic RRS takes place at 800 K in air (see Fig. 7a) and the  $\bar{y}'(zz)y'$  spectrum measured after subsequent cooling down to room temperature contains a weak Raman scattering  $\sim 587 \text{ cm}^{-1}$  attributed to  $\text{CFe}^{3+}\text{O}_6$  due to trapped



**Fig. 4 Polarized Raman spectra of grunerite A85 measured at 300 K after annealing in air to the temperature indicated and subsequently cooled down.** **a** Data collected in  $\bar{y}'(zz)y'$  scattering geometry; **b** data collected in  $\bar{y}'(x'x')y'$  scattering geometry. Spectra are vertically offset for clarity. The dashed lines in the upper plot trace the corresponding new Raman scattering signals  $-273$ ,  $470$ , and  $576$   $\text{cm}^{-1}$  appearing at  $700$  K in  $\bar{y}'(zz)y'$  spectra; the negligible room-temperature intensity of the Raman scattering  $-815$   $\text{cm}^{-1}$  observed at elevated temperatures indicates that this signal originates from multi-phonon excitation.

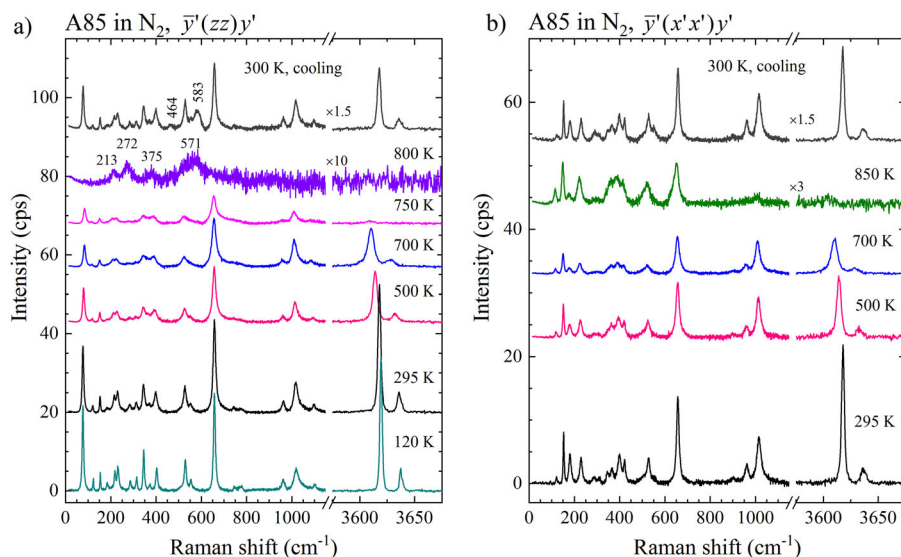
electrons, resembling the spectral features observed for A85 when heating in air up to  $700$  K (see Fig. 2a). Also, the OH-stretching peaks in the  $\bar{y}'(zz)y'$  spectrum of A86 measured in  $\text{N}_2$  disappear at  $850$  K (Fig. 7c), similarly to the corresponding spectrum at  $750$  K for A85 (Fig. 6a). Following this trend, one should expect sample A86 to exhibit  $\bar{y}'(zz)y'$  RRS in  $\text{N}_2$   $\sim 900$  K, but due to instrumental limitations this temperature could not be reached in our experiment. The complete recovery of the  $\bar{y}'(x'x')y'$  spectrum of A86 after heating in air up to  $950$  K (Fig. 7b) demonstrates that the temperature of irreversible Fe oxidation has not been reached. This further emphasizes the importance of our results for potential technological applications based on materials comprising quasi one-dimensional octahedral systems.

At last, we have considered the temperature evolution of the  $\text{SiO}_4$ -ring mode  $\omega_{\text{ring}} \sim 660$   $\text{cm}^{-1}$  as well as of the  $\text{SiO}_4$ -chain mode  $\omega_{\text{chain}} \sim 78$   $\text{cm}^{-1}$  in the range  $100$ – $950$  K (Fig. 8). Both modes appear at slightly lower wavenumbers for A85 than for A86 due to its higher  $^{\text{C}}\text{Fe}^{2+}$  content<sup>27</sup>. A minimum in  $\omega_{\text{ring}}(T)$  marks the temperature of  $\text{SiO}_4$ -ring modification to adopt the smaller  $\text{Fe}^{3+}\text{O}_6$  volume, triggering the release of  $e^-$  and  $\text{H}^+$  from the crystal, that is, the irreversible  $^{\text{C}}\text{Fe}$  oxidation<sup>13</sup>. The threshold temperature of irreversible oxidation  $T_{\text{irr.ox}}$  is not reached for A86

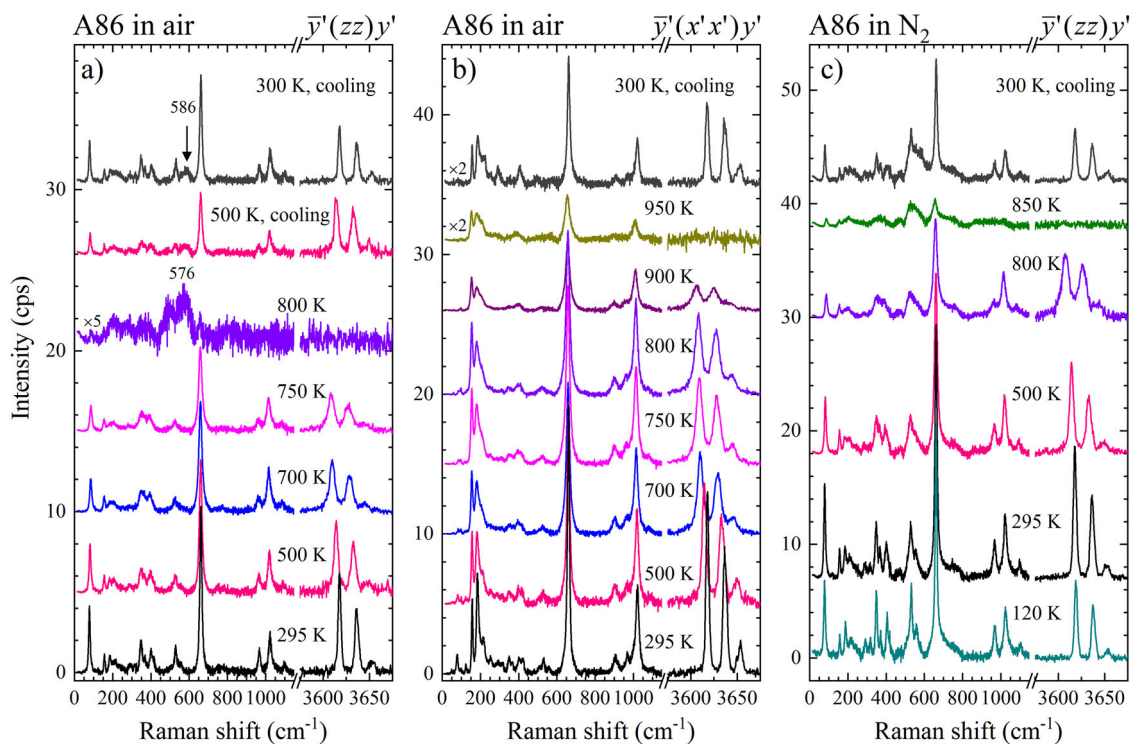


**Fig. 5 Temperature dependence of the integrated intensity of selected peaks for grunerite A85.** **a** Intensity ratio of the strongest RRS peak ( $-586$   $\text{cm}^{-1}$ ) and the non-RRS peak generated by ring mode ( $-658$   $\text{cm}^{-1}$ )  $I_{586}^{\text{RRS}} / (I_{586}^{\text{RRS}} + I_{\text{ring mode}})$ , derived from the  $\bar{y}'(zz)y'$  spectra measured at room temperature after heating in air to a certain temperature  $T_{\text{heat}}$ ; the line is a Boltzmann fit to the data points. **b** Fractional intensity  $I_n$  of the Raman-active  $\text{MO}_6$  mode  $-152$   $\text{cm}^{-1}$  in the  $\bar{y}'(x'x')y'$  spectra measured in situ in air.

in the studied  $T$  range (Fig. 8a), whereas  $T_{\text{irr.ox}}$  is  $850$  K for A85, in excellent agreement with the value derived from the temperature dependencies of  $I_{586}^{\text{RRS}} / (I_{586}^{\text{RRS}} + I_{\text{ring mode}})$  and  $I_n(152)$  (Fig. 5). At low temperatures,  $\omega_{\text{ring}}(T)$  reaches a saturation, indicating no further change within the silicate double chains; however  $\omega_{\text{chain}}(T)$  exhibits a broad minimum  $\sim 170$  K (Fig. 8b), suggesting a rearrangement of the double chain with respect to the  $M(4)$  site. A minimum in the wavenumber of a low-energy phonon points to a phase transition, especially when we know that this particular phonon mode is sensitive to the symmetry of the crystal structure<sup>27</sup>. Following the concepts of hard-mode spectroscopy<sup>38</sup>, we attribute the minimum in  $\omega_{\text{chain}}(T)$  to a  $P2_1/m \leftrightarrow C2/m$  phase transition of mixed displacive and order/disorder character, which has been already observed for cummingtonite<sup>26</sup>. The phase transition temperature  $T_c$  depends on the total content of  $\text{Fe}^{2+}$  and for  $x = \text{Fe}/(\text{Fe} + \text{Mg})$  ranging between 0 and 0.45,  $T_c$  varies between  $\sim 600$  and  $200$  K<sup>26</sup>. A linear extrapolation to  $T_c(x)$  suggests that grunerite with  $x$  above 0.7 should not undergo a phase transition to  $P2_1/m$  in agreement with the data provided by infrared spectroscopy or XRD<sup>26</sup>. Our Raman data however clearly indicate a structural instability in the silicate chain, which commonly leads to a  $P2_1/m$ – $C2/m$  symmetry change in both amphiboles and pyroxenes<sup>39,40</sup>, suggesting that  $T_c(x)$  follows a more complex trend. The small depth in  $\omega_{\text{chain}}(T)$  around the minimum suggests only subtle structural alteration, which could explain why such a phase transition has not been reported so far for grunerite.



**Fig. 6** Temperature-dependent polarized Raman spectra of grunerite A85 measured in situ in  $N_2$  atmosphere. **a** Data collected in  $\bar{y}'(zz)y'$  scattering geometry; **b** data collected in  $\bar{y}'(x'x')y'$  scattering geometry. Spectra are vertically offset for clarity.

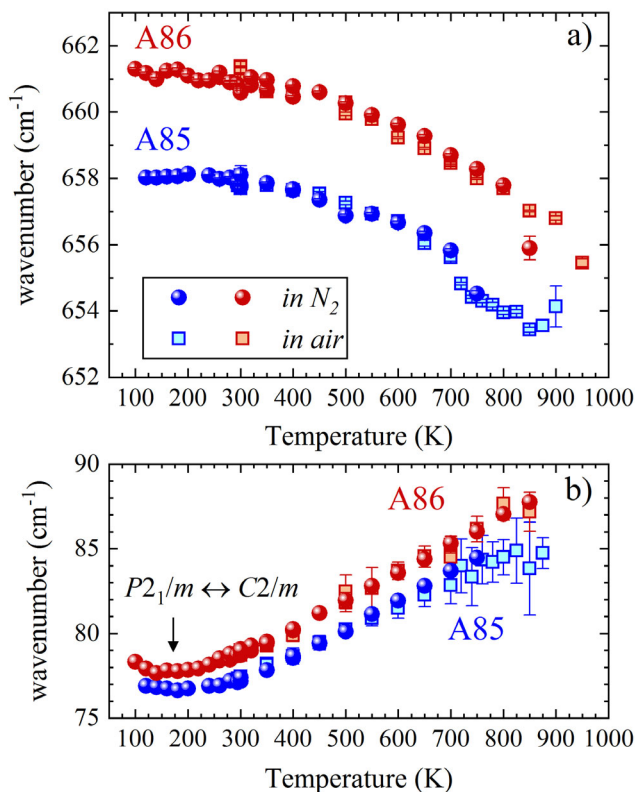


**Fig. 7** Temperature-dependent Raman spectra of grunerite A86 measured in situ. **a** Data collected in air in  $\bar{y}'(zz)y'$  scattering geometry; **b** data collected in air in  $\bar{y}'(x'x')y'$  scattering geometry; **c** data collected in  $N_2$  in  $\bar{y}'(zz)y'$  scattering geometry. Spectra are vertically offset for clarity.

## Discussion

Seismic and electromagnetic anomalies in subduction zones have triggered continuously growing interest on amphiboles and layer silicates, as well as of hydrogen-bearing nominally anhydrous minerals, as responsible for the electrical conductivity of the mid-crust and subduction zones<sup>16–18,41–46</sup>. Metasomatic processes leading to the formation of hydrous fluids may considerably contribute to the anomalies in lithospheric conductivity<sup>22,44</sup>. However, recent studies have indicated that conductive aqueous fluids alone cannot explain the anisotropic conductivity observed in some locations<sup>16,42</sup>. Moreover, although the geophysical

anomalies generally depend on both temperature and pressure as thermodynamical parameters<sup>47,48</sup>, temperature rather than pressure is the major factor influencing the electrical conductivity of rock-forming minerals<sup>16,22,46</sup>. Two main temperature-activated solid-state processes have been considered to cause the rock conductivity: (i) hopping of electrons/electron holes between ferrous and ferric iron and (ii) diffusion of  $H^+$ <sup>44</sup>. The former process presumes the presence of minerals with mixed-valent Fe state, that is, with coexisting  $Fe^{2+}$  and  $Fe^{3+}$  in the nominal formula, like riebeckite or arfvedsonite, leading to polaron conductivity<sup>16,45</sup>. An additional process, postulated for Fe-free minerals, involves



**Fig. 8** Temperature dependence of the wavenumber of selected modes for A85 and A86. **a** Trends for the ring mode; **b** trends for the chain mode. Data points derived from the  $\bar{y}(zz)'$  spectra measured in situ in  $N_2$  atmosphere are given with circles; data points derived from  $\bar{y}(x'x')'$  spectra measured in situ in air are given with squares. Blue symbols refer to A85, red symbols to A86.

primarily the ionic conduction: this mechanism is characterized by high activation energy ( $>2$  eV) and has been inferred to explain the conductivity of tremolite at very high temperatures<sup>46</sup>.

As discussed above, the essence of RRS based on Fröhlich-type interactions is the formation of polarons, i.e., coupled electrons and LO phonons, allowing for the propagation of the associated local structural distortion, that is, the  $MO_6$  shrinking in the present case. Our study directly demonstrates the existence of polarons in amphiboles at high temperature; so far this process has been only assumed to be responsible for the electrical conductivity in Fe-bearing rock-forming silicates<sup>16,45</sup>, mainly based on the observed low activation energies ( $<1$  eV) for these compounds. The observed anisotropic RRS undoubtedly shows direction-dependent temperature activation of polarons, in full accordance with the measured anisotropic conductivity of amphiboles, being five to six times higher along the  $c$  axis than along the perpendicular direction<sup>17,18,45</sup>. Moreover, our results demonstrate that mixed-valent Fe state is not necessary for the development of polaron conductivity. In fact, high temperatures naturally lead to delocalized electrons coupled with LO phonons also in amphiboles containing (at room temperature) only divalent Fe. The structural similarity between amphiboles and layer silicates (both consisting of  $MO_6$  slabs linked to  $TO_4$  slabs) suggests that the same process may occur in both structure types. Therefore, our work allows the general conclusion that anisotropically coupled electron and phonon excitations provide a robust explanation for the anisotropic conductivity of lithospheric rocks containing hydrous Fe-bearing silicates.

Diffusion of  $H^+$  as a possible source for the rock conductivity has been always considered in terms of irreversible

dehydrogenation and related to the oxygen fugacity. Our results reveal that delocalized  $H^+$ , hopping between different W anions, do exist in both oxygen-containing and oxygen-poor/free surroundings, although the final expulsion of  $H^+$  from the structure, in the form of water molecules (“dehydration”, a process different from “dehydrogenation”) is only possible in the presence of external oxygen. This conclusion is quite important in petrology/geophysics, because of its key role for the better understanding of water recycling in the mantle. The Raman analysis of both sodium amphiboles<sup>13</sup> and Mg-Fe-Mn amphiboles (this study) suggests that the formation of delocalized  $e^-$  promotes the delocalization of  $H^+$ , but there is no evidence that the motion of polarons within the crystal bulk is coupled to  $H^+$  motion, implying that polaron migration may occur also in oxo-amphiboles. Further studies are necessary to clarify whether the  $H^+$  hopping is realized predominantly within one octahedral strip or between adjacent strips. Our very recent kinetic study of riebeckite (results not yet published) indicates that the diffusion of  $H^+$  across the amphibole crystal bulk is faster perpendicular to the  $c$  axis rather than along the  $c$  axis, suggesting  $H^+$  hopping between strips. Another point to be explored in follow-up studies is whether delocalization of  $H^+$  is hindered in OH-amphiboles having a filled A site.

It is worth noting that an increase in conductivity has been observed above the temperature of dehydration of amphiboles<sup>16</sup>, i.e., after the injection of  $e^-$  and  $H^+$  from the crystal bulk. The irreversible formation of  $Fe^{3+}$  certainly changes the whole electron band structure and the energy gap slightly shrinks<sup>14</sup>. Therefore, in this case the number of thermally activated conduction electrons in total should be larger than when the  $Fe^{2+}$ – $Fe^{3+}$  exchange is dynamic (reversible), but the mechanism beyond conductivity, namely coupled electron–phonon excitations is the same.

## Conclusions

The appearance of anisotropic RRS at elevated temperatures directly evidences the formation of temperature-activated polarons involving an electron transition between hybridized O  $2p$  and Fe  $3d$  levels with a dipole moment along the octahedral strips in the amphibole structure. These anisotropically coupled electron and phonon excitations in hydrous Fe-bearing chain/layered silicates are the atomistic source of anisotropic lithospheric conductivity, rather than phenomena limited to solid–fluid interfaces.

The presence of mobile electronic polarons and  $H^+$  cations at temperatures above 700 K, which are typical of the lithosphere and forearc regions of slab–mantle wedge interfaces in subduction zones, indicate that both types of charge carriers can contribute to the overall lithospheric conductivity.

The occurrence of either type of charge carriers does not require the initial coexistence of ferrous and ferric iron in the mineral and does not depend on the oxygen fugacity of the system. The presence of external oxygen is however required to trigger  $H^+$  expulsion as  $H_2O$  molecules, thus making the amphibole an efficient carrier of water into the crust/mantle.

## Methods

**Sample characterization.** The chemical composition was analyzed by wavelength-dispersive electron–microprobe (Supplementary Note 1, Supplementary Table 1). The oxidation state of iron and the site populations were further checked by Mössbauer spectroscopy (Supplementary Note 2, Supplementary Figure 1 and Supplementary Table 2). The room-temperature structure was refined to single-crystal XRD data (Supplementary Note 3, Supplementary Table 3, Supplementary Data 1, and Supplementary Data 2). The chemical formulae were calculated using the Excel sheet developed by Locock<sup>49</sup>, taking into account the  $Fe^{2+}$  site population from the structure refinements and Mössbauer data. Euhedral crystal grains of size  $\sim 0.1 \times 0.1 \times 0.5$  mm<sup>3</sup> with the prim axis along the crystallographic [001] direction and natural crystal faces parallel to the common cleavage planes ( $\{110\}$  or  $\{010\}$ ) were used in the Raman spectroscopic experiments. Pristine grains of similar size have been used for each temperature run.



**Raman spectroscopy.** The Raman spectra were collected with a Horiba Jobin-Yvon T64000 triple-monochromator spectrometer equipped with an Olympus BX41 microscope and a liquid-N<sub>2</sub>-cooled charge-couple-device detector, using the 514.532-nm line of a Coherent Innova 90 C FreD Ar<sup>+</sup> laser. The spectrometer was calibrated to the Si Raman peak at 520.5 cm<sup>-1</sup>. The spectral resolution was ~1.9 cm<sup>-1</sup>, whereas the instrumental precision in determining the peak positions was ~0.35 cm<sup>-1</sup>. Prior and after the temperature runs, spectra were also collected with the 488-nm laser line, to verify the phonon origin of the peaks observed. In situ temperature-dependent experiments in N<sub>2</sub> atmosphere were performed by a LINKAM THMS-E600, whereas in air with a LINKAM TS1200 EV-1015. Detailed information about the temperature ramps is given in Supplementary Table 4. The as-measured spectra were baseline-corrected, temperature-reduced for the Bose-Einstein population factor, and fitted with pseudo-Voigt functions (see Supplementary Note 4).

**DFT calculations.** The electron band structure and DOS were calculated using the DFT based on the generalized gradient approximation of Perdew-Burke-Ernzerhof as implemented in the Vienna Ab-initio Simulation Package<sup>50</sup>. The electron and core interactions are included using the frozen-core projector augmented wave method, with the plane-wave cutoff energy chosen as 360 eV for model structures (see also Supplementary Note 5). The lattice constants and the atom coordinates are optimized until the convergence of the force on each atom is <0.01 eV/Å. The Monkhorst-Pack scheme is used to sample the Brillouin zone. The structures are fully relaxed with a mesh of 4 × 2 × 6. The number of bands per *k* point was set to 10 during the electronic band structure calculations.

### Data availability

The data sets generated during and/or analyzed during the current study are available from the corresponding author on reasonable request.

Received: 10 December 2020; Accepted: 7 May 2021;

Published online: 03 June 2021

### References

- Hawthorne, F. C. & Oberti, R. Amphiboles: crystal chemistry. *Rev. Mineral. Geochem.* **67**, 1–54 (2007).
- Deer, W. A., Howie, R. A. & Zussman, J. *Double-chain silicates*, 2nd edn. The Geological Society, pp 764 (1997).
- Darby Dyar, M., Mackwell, S. J., McGuire, A. V., Cross, L. R. & Robertson, G. D. Crystal chemistry of Fe<sup>3+</sup> and H<sup>+</sup> in mantle kaersutite: implications for mantle metasomatism. *Am. Mineral.* **78**, 968–979 (1993).
- McCammon, C. A. et al. Oxidation state of iron in hydrous mantle phases: implications for subduction and mantle oxygen fugacity. *Phys. Earth Planet. Inter.* **143–144**, 157–169 (2004).
- Welch, M. D., Cámara, F., Della Ventura, G. & Iezzi, G. In situ non-ambient studies of amphiboles. *Rev. Mineral.* **67**, 223–260 (2007).
- Mu, S., Pan, M. & Yuan, R. Z. A new concept: hydrogen storage in minerals. *Mater. Sci. Forum* **475–479**, 2441–2444 (2005).
- Kumar, R., Lohani, M., Bhusan, A. & Rahman, Q. Cyto-genotoxicity of amphibole asbestos fibers in cultured human lung epithelial cell line: role of surface iron. *Toxicol. Ind. Health* **26**, 57582 (2010).
- Addison, W. E. & Sharp, J. H. A mechanism for the oxidation of ferrous iron in hydroxylated silicates. *Clay Miner. Bull.* **5**, 73–79 (1962).
- Clark, M. W. & Freeman, A. G. Kinetics and mechanism of dihydroxylation of crocidolite. *Trans. Faraday Soc.* **63**, 2051–2056 (1967).
- Popp, R. K., Virgo, D., Yoder, H. S., Hoering, T. C. & Phillips, M. W. An experimental study of phase equilibria and Fe oxy-component in kaersutitic amphibole, implications for the H<sub>2</sub> and H<sub>2</sub>O in the upper mantle. *Am. Mineral.* **80**, 534–548 (1995).
- Oberti, R., Boiocchi, M. & Zema, M. Thermoelasticity, cation exchange, and deprotonation in Fe-rich holquistite: toward a crystal-chemical model for the high-temperature behavior of orthorhombic amphiboles. *Am. Mineral.* **104**, 1829–1839 (2019).
- Della Ventura, G. et al. Deprotonation of Fe-dominant amphiboles: single-crystal HT-FTIR spectroscopic studies of synthetic potassic-ferro-richterite. *Am. Mineral.* **102**, 117–125 (2017).
- Della Ventura, G. et al. The dynamics of Fe oxidation in riebeckite: a model for amphiboles. *Am. Mineral.* **103**, 1103–1111 (2018).
- Della Ventura, G. et al. Iron oxidation dynamics vs. temperature of synthetic potassic-ferro-richterite: a XANES investigation. *Phys. Chem. Chem. Phys.* **20**, 21764–21771 (2018).
- Galdenzi, F., Della Ventura, G., Cibin, G., Macis, S. & Marcelli, A. Accurate Fe<sup>3+</sup>/Fe<sub>tot</sub> ratio from XAS spectra at the Fe K-edge. *Radiat. Phys. Chem.* **175**, 108088 (2018).
- Hu, H., Dai, L., Li, H., Sun, W. & Li, B. Effect of dehydrogenation on the electrical conductivity of Fe-bearing amphibole: Implications for high conductivity anomalies in subduction zones and continental crust. *Earth Planet. Sci. Lett.* **498**, 27–37 (2018).
- Schmidbauer, E., Kunzmann, T. H., Fehr, T. H. & Hochleitner, R. Electrical conductivity, thermopower and <sup>57</sup>Fe Mössbauer spectroscopy on an Fe-rich amphibole, arfvedsonite. *Phys. Chem. Miner.* **23**, 99–106 (1996).
- Schmidbauer, E., Kunzmann, T. H., Fehr, T. H. & Hochleitner, R. Electrical resistivity and <sup>57</sup>Fe Mössbauer spectra of Fe-bearing calcic amphiboles. *Phys. Chem. Miner.* **27**, 347–356 (2000).
- Biedermann, A. R., Koch, C. B., Pettko, T. & Hirt, A. M. Magnetic anisotropy in natural amphibole crystals. *Am. Mineral.* **100**, 1940–1951 (2015).
- Biedermann, A. R., Kunze, K. & Hirt, A. M. Interpreting magnetic fabrics in amphibole-bearing rocks. *Tectonophysics* **722**, 566–576 (2018).
- Wang, D., Guo, Y., Yu, Y. & Karato, S. Electrical conductivity of amphibole-bearing rocks: influence of dehydration. *Contrib. Mineral. Petrol.* **164**, 17–25 (2012).
- Hu, H., Dai, L., Li, H., Hui, K. & Sun, W. Influence of dehydration on the electrical conductivity of epidote and implications for high-conductivity anomalies in subduction zones. *J. Geophys. Res. Solid Earth* **122**, 2751–2762 (2017).
- Brovarone, A. V. et al. Massive production of abiotic methane during subduction evidenced in metamorphosed ophiocarbonates from the Italian Alps. *Nat. Commun.* **8**, 14134 (2017).
- Hawthorne, F. C. et al. Nomenclature of the amphibole supergroup. *Am. Mineral.* **97**, 2031–2048 (2012).
- Boffa Ballaran, T., Carpenter, M. A. & Domeneghetti, M. C. Phase transition and mixing behavior of the cummingtonite-grunerite solid-solution. *Phys. Chem. Mineral.* **28**, 87–101 (2001).
- Boffa Ballaran, T., Carpenter, M. A. & Domeneghetti, M. C. Order parameter variation through the C2/m-P2<sub>1</sub>/m phase transition in cummingtonite. *Am. Mineral.* **89**, 1717–1727 (2004).
- Waeselmann, N. et al. Non-destructive determination of the amphibole crystal chemistry by Raman spectroscopy; one step closer. *J. Raman Spectrosc.* **51**, 1530–1548 (2020).
- Stangarone, C., Tribaudino, M., Prencipe, M. & Lottici, P. P. Raman modes in Pbc<sub>2</sub> enstatite (Mg<sub>2</sub>Si<sub>2</sub>O<sub>6</sub>): an assignment by quantum mechanical calculation to interpret experimental results. *J. Raman Spectrosc.* **47**, 1247–1258 (2016).
- Kroumova, E. et al. Bilbao crystallographic server: useful databases and tools for phase-transition studies. *Phase Transitions* **76**, 155–170 (2003).
- Yu, P. Y. & Cardona, M. *Fundamentals of Semiconductors* (Springer, 2010).
- de la Flor, G. et al. Resonance Raman scattering of perovskite-type relaxor ferroelectrics under non-ambient conditions. *Phys. Rev. B* **90**, 064107 (2014).
- Vitova, T. et al. X-ray absorption spectroscopy of Ru-doped relaxor ferroelectrics with a perovskite-type structure. *Phys. Rev. B* **89**, 144112 (2014).
- Rohrbeck, A. et al. The effect of chemical variations on the structural polarity of relaxor ferroelectrics studied by resonance Raman spectroscopy. *J. Phys. Condens. Matter.* **28**, 475902 (2016).
- Ivanov, V. G., Dylugov, M. & Oberti, R. Polarized Raman spectroscopy and lattice dynamics of potassicmagnesian-arfvedsonite. *Phys. Chem. Mineral.* **46**, 181–191 (2019).
- Alexandrov, V. & Rosso, K. M. Electron transport in pure and substituted iron oxyhydroxides by small-polaron migration. *J. Chem. Phys.* **140**, 234701 (2014).
- Holstein, T. Studies of polaron motion Part II. The “Small” polarons. *Ann. Phys.* **8**, 343–389 (1959).
- Robie, R. A. Debye temperatures of selected silicate minerals. *U.S. Geological Survey Open-File Report* 88–663 (1988).
- Bismayer, U. Hard mode Raman spectroscopy and its application to ferroelastic and ferroelectric phase transitions. *Phase Transitions* **27**, 211–267 (1990).
- Prewitt, C. T., Papike, J. J. & Ross, M. Cummingtonite: a reversible nonquenchable transition from P2<sub>1</sub>/m to C2/m symmetry. *Earth Planet. Sci. Lett.* **8**, 448–450 (1970).
- Smith, J. V. Crystal structure and stability of MgSiO<sub>3</sub> polymorphs: physical properties and phase relations of Mg,Fe pyroxenes. *Mineral. Mag. Spec. Paper* **2**, 3–29 (1969).
- Hirsch, L. M., Shankland, T. J. & Duba, A. G. Electrical conduction and polaron mobility in Fe-bearing olivine. *Geophys. J. Int.* **114**, 36–44 (1993).
- Yoshino, T., Matsuzaki, T., Yamashita, S. & Katsura, T. Hydrous olivine unable to account for conductivity anomaly at the top of the asthenosphere. *Nature* **443**, 973–976 (2006).
- Reynard, B., Mibe, K. & Van de Moortèle, B. Electrical conductivity of the serpentinized mantle and fluid flow in subduction zones. *Earth Planet. Sci. Lett.* **307**, 387–394 (2011).
- Yoshino, T. & Katsura, T. Electrical conductivity of mantle minerals: role of water in conductivity anomalies. *Annu. Rev. Earth Planet. Sci.* **41**, 605–628 (2013).

45. Wang, D., Guo, Y., Yu, Y. & Karato, S. Electrical conductivity of talc aggregates at 0.5 GPa: influence of dehydration. *Phys. Chem. Miner.* **40**, 11–17 (2013).
46. Shen, K., Wang, D. & Liu, T. Electrical conductivity of tremolite under high temperature and pressure: implications for the high-conductivity anomalies in the Earth and Venus. *Contrib. Mineral. Petrol.* **175**, 52 (2020).
47. Abers, G. A. & Hacker, B. R. A MATLAB toolbox and Excel workbook for calculating the densities, seismic wave speeds, and major element composition of minerals and rocks at pressure and temperature. *Geochem. Geophys. Geosyst.* **17**, 616–624 (2016).
48. Peng, Y. & Mookherjee, M. Thermoelasticity of tremolite amphibole: geophysical implications. *Am. Mineral.* **105**, 904–916 (2020).
49. Locock, A. J. An Excel spreadsheet to classify chemical analyses of amphiboles following the IMA 2012 recommendations. *Comput. Geosci.* **62**, 1–11 (2014).
50. Kresse, G. & Furthmüller, J. Efficiency of ab-initio total energy calculations for metals and semiconductors using a plane-wave basis set. *Comput. Mat. Sci.* **6**, 15–50 (1996).
51. Momma, K. & Izumi, F. Vesta: a three-dimensional visualization system for electronic and structural analysis. *J. Appl. Crystallogr.* **41**, 653–658 (2008).
52. Della Ventura, G., Mihailova, B. & Hawthorne, F. C. Raman and FTIR spectroscopy of synthetic amphiboles: II. Divalent (Mg,Co) substitution at the octahedral site. *Can. Mineral.* **59**, 1–15 (2020).

### Acknowledgements

Financial support by the Deutsche Forschungsgemeinschaft (MI 1127/7-2) is gratefully acknowledged. G.D.V. was supported by the grant to Department of Science, Roma Tre University (MIUR-Italy Dipartimenti di Eccellenza, ARTICOLO 1, COMMI 314-337 LEGGE 232/2016). W.X. is financially supported by the National Science Foundation of China (Grant #12075273); the DFT results were partially obtained on the Era petascale supercomputer of the Computer Network Information Center of Chinese Academy of Sciences.

### Author contributions

B.M., G.D.V., J.S., and R.O. planned and developed the original project. B.M. analyzed the Raman data. G.D.V. provided the samples and performed electron–microprobe analysis. N.W. collected the Raman data. W.X. performed the DFT calculations. J.S. helped with the spectroscopic analyses. FG helped with the sample characterization. A.M. helped with the DFT analysis. G.J.R. performed the Mössbauer analysis. M.B. collected

the XRD data. R.O. interpreted the structure-refinement data. B.M. and G.D.V. wrote the manuscript. All authors reviewed the manuscript.

### Funding

Open Access funding enabled and organized by Projekt DEAL.

### Competing interests

The authors declare no competing interests.

### Additional information

**Supplementary information** The online version contains supplementary material available at <https://doi.org/10.1038/s43246-021-00161-y>.

**Correspondence** and requests for materials should be addressed to B.M.

**Peer review information** Primary handling editor: Aldo Isidori

**Reprints and permission information** is available at <http://www.nature.com/reprints>

**Publisher's note** Springer Nature remains neutral with regard to jurisdictional claims in published maps and institutional affiliations.



**Open Access** This article is licensed under a Creative Commons Attribution 4.0 International License, which permits use, sharing, adaptation, distribution and reproduction in any medium or format, as long as you give appropriate credit to the original author(s) and the source, provide a link to the Creative Commons license, and indicate if changes were made. The images or other third party material in this article are included in the article's Creative Commons license, unless indicated otherwise in a credit line to the material. If material is not included in the article's Creative Commons license and your intended use is not permitted by statutory regulation or exceeds the permitted use, you will need to obtain permission directly from the copyright holder. To view a copy of this license, visit <http://creativecommons.org/licenses/by/4.0/>.

© The Author(s) 2021